Pressure-induced suppression of Wigner-crystal antiferromagnetic state in $La_{0.33}Ca_{0.67}MnO_3$

D. P. Kozlenko,[1] L. S. Dubrovinsky,[2] B. N. Savenko,[1] V. I. Voronin,[3] E. A. Kiselev,[3] and N. V. Proskurnina[3]
[1]*Frank Laboratory of Neutron Physics, JINR, 141980 Dubna, Russia*
[2]*Bayerisches Geoinstitut, Universität Bayreuth, Bayreuth D-95440, Germany*
[3]*Institute for Metal Physics, Ural Division of RAS, 620219 Yekaterinburg, Russia*
(Received 29 October 2007; revised manuscript received 4 March 2008; published 31 March 2008)

The crystal and magnetic structures of $La_{0.33}Ca_{0.67}MnO_3$ were studied at high pressures up to 50 and 5 GPa, respectively. The lattice contraction is highly anisotropic with the most compressible *b* axis. A rapid suppression of the "Wigner-crystal" antiferromagnetic (AFM) state and stabilization of the *C*-type AFM state under high pressure were observed. Possible reasons for the instability of the Wigner-crystal AFM state under pressure are discussed.

DOI: 10.1103/PhysRevB.77.104444 PACS number(s): 71.30.+h, 61.50.Ks, 75.25.+z

I. INTRODUCTION

Perovskite manganites $R_{1-x}A_xMnO_3$ (*R*, rare earth; *A*, alkali earth elements) are at the current focus of extensive scientific research due to a rich variety of fascinating physical phenomena—colossal magnetoresistance, insulator-metal transition, charge and orbital ordering, and mesoscopic phase separation.[1,2] A complicated balance of ferromagnetic (FM) double exchange mediated by charge carriers of e_g nature and antiferromagnetic (AFM) superexchange interactions between localized magnetic moments of t_{2g} nature coupled to lattice distortion effects and orbital degrees of freedom leads to an especially complex phase diagram of compounds with $x>0.5$.

Manganites $R_{1-x}Sr_xMnO_3$ (*R*=La, Pr, and Nd) with a larger average *A*-site ionic radius $\langle r_A\rangle$ exhibit AFM states of *A* type for $x\sim 0.5-0.6$ and *C* type for $x\sim 0.6-0.85$ concentration range.[3–5] In the *A*-type AFM state, Mn magnetic moments form FM planes with AFM coupling between them, while in the *C*-type AFM state, they form linear FM chains with AFM interchain coupling.[3–5] In compounds $R_{1-x}Ca_xMnO_3$ (*R*=La, Pr, and Nd) with a smaller $\langle r_A\rangle$, charge localization effects become more pronounced and, for *x* values corresponding to ideal ratios of Mn^{3+} and Mn^{4+} ions—1:1, 2:3, etc., a number of more complicated AFM ground states occur, e.g., CE-type AFM ($x=0.5$) and "Wigner-crystal" (WC, $x=0.67$) AFM ones.[6–13] The characteristic feature of these states is the presence of two structurally and magnetically inequivalent sublattices, corresponding either to different propagation vectors $k_C=(1/2\ 0\ 1/2)$ and $k_E=(0\ 0\ 1/2)$ for the CE-type AFM state or the same propagation vector $k_{WC}=(1/3\ 0\ 1/2)$ for the WC AFM state. One of these sublattices exhibits a cooperative Jahn–Teller distortion of MnO_6 octahedra associated with the $d(3x^2-r^2)/d(3z^2-r^2)$ e_g orbital order, while another one has a more regular MnO_6 octahedra.[6–13] In both the CE-type and WC AFM states, Mn magnetic moments form quasi-one-dimensional zigzag FM chains with AFM interchain coupling with a somewhat different chain topology.[8,10,14] Traditionally, the formation and properties of CE-type and WC AFM states have been interpreted in terms of the long range Mn^{3+}/Mn^{4+} charge ordering concept,[6–13] although some recent results imply that the real valence modulation between inequivalent Mn sites is much smaller than $(3.5\pm 0.5)e$.[15–19]

The temperature T_{CO} corresponding to the onset of the lattice distortions associated with charge ordering rapidly grows from 155 to 260 K with increasing Ca content (and Mn^{4+} ion concentration) in the $x=0.5-0.67$ range for the $La_{1-x}Ca_xMnO_3$ system and it starts to decrease for larger *x* values, while the Néel temperature weakly decreases, $T_N\sim 155-140$ K.[8–11] The WC AFM state of $La_{1-x}Ca_xMnO_3$ with $x\sim 2/3$ remains stable in high magnetic fields *H* of up to 14 T, while the CE-type AFM state for $x\sim 1/2$ is gradually suppressed at $H\sim 6$ T.[20]

A study of high pressure effects on the $La_{1-x}Ca_xMnO_3$ system can provide an important insight into the formation of ground states of manganites with an enhanced charge localization and their stability with respect to a variation of interatomic distances and angles, controlling the balance of competing interactions. Recently, it was found that the CE-type AFM state remains stable in $La_{0.5}Ca_{0.5}MnO_3$ with increasing T_{CO} and T_N values at high pressure, resulting in a monoclinic distortion of the crystal structure,[21] and a similar tendency seems to be realized in $Nd_{0.5}Ca_{0.5}MnO_3$ as well.[22] Unlike half-doped systems, the high pressure effects on manganites with more complex AFM states realized for $x\sim 2/3$ remain unexplored. In the present study of the crystal and magnetic structures of the $La_{0.33}Ca_{0.67}MnO_3$ compound with the largest T_{CO} for the $La_{1-x}Ca_xMnO_3$ family, we demonstrate that the WC AFM state in this case is remarkably unstable to the application of a high external pressure and is completely destroyed in favor of the *C*-type AFM state, which is a ground state for manganites with larger radii $\langle r_A\rangle$.

II. EXPERIMENTAL DETAILS

The $La_{0.33}Ca_{0.67}MnO_3$ sample was synthesized by a standard solid state reaction method. The initial reagents were La_2O_3, $CaCO_3$, and MnO_2. La_2O_3 was preliminarily annealed at 1200 °C for 2 h, $CaCO_3$ at 500 °C for 3 h, and MnO_2 at 750 °C for 24 h. The latter process involved the transition from MnO_2 to Mn_2O_3. A mixture of the oxides was taken in the necessary stoichiometric proportion and thoroughly ground in ethanol. The mixture was annealed in four steps, with intermediate grinding in ethanol every 20 h: the first stage was annealing at 850 °C for 20 h, the second stage

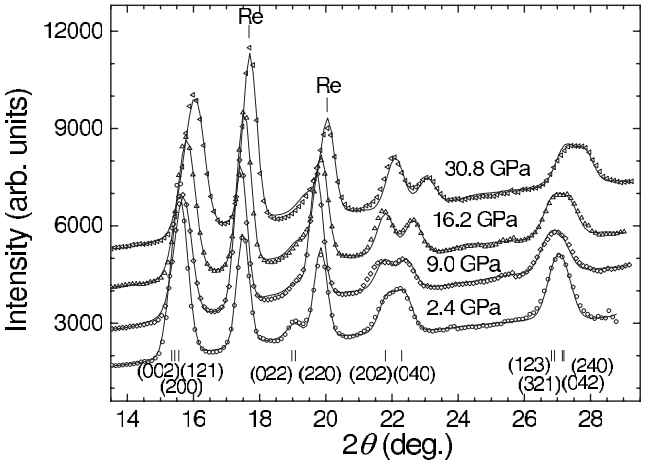

FIG. 1. X-ray diffraction patterns of $La_{0.33}Ca_{0.67}MnO_3$ measured at selected pressures and ambient temperature and processed by the Rietveld method. Experimental points and calculated profiles are shown.

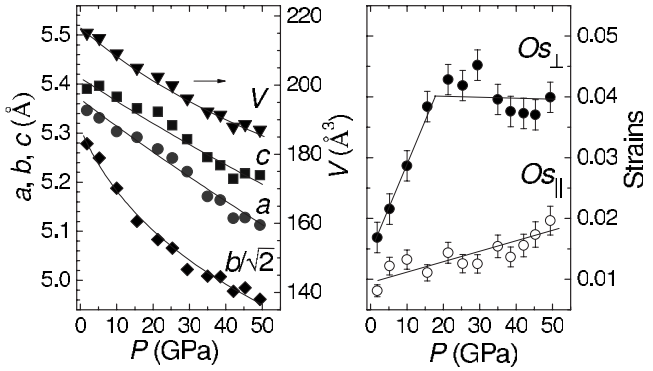

FIG. 2. Lattice parameters and unit cell volume (left) and orthorhombic strains (right) in $La_{0.33}Ca_{0.67}MnO_3$ as functions of pressure.

at 950 °C for 20 h, the third stage at 1100 °C for 100 h, and the fourth stage at 1200 °C for 200 h. Then, the sample was quenched in cooling to room temperature. The x-ray diffraction (XRD) measurements at ambient conditions showed that the sample has a single orthorhombic phase of *Pnma* symmetry.

XRD measurements at high pressures up to 50 GPa were conducted at ambient temperature in four-pin-type diamond anvil cells.[23] The Re gasket and LiF admixed to a sample as a pressure transmitting medium were used. The XRD spectra were measured by using a high-brilliance FRD rotating anode generator (Mo $K\alpha$ radiation, $\lambda=0.7115$ Å), FluxMax focusing optics, and a Bruker APEX charge coupled device area detector. The two-dimensional XRD images were converted to conventional one-dimensional diffraction patterns by using the FIT2D program.[24] The data analysis was performed by using the GSAS program.[25]

Neutron diffraction measurements were performed at the DN-12 spectrometer by using sapphire anvil cells[26] in the 10–300 K temperature range at high pressures of up to 5 GPa. Diffraction patterns were collected at scattering angles of 45.5° and 90° with the resolution $\Delta d/d=0.022$ and 0.015, respectively. Experimental data were analyzed by the Rietveld method using the MRIA program[27] or FULLPROF (Ref. 28) if magnetic structure was to be included.

III. RESULTS AND DISCUSSION

At ambient conditions, $La_{0.33}Ca_{0.67}MnO_3$ has an orthorhombically distorted perovskite crystal structure (space group *Pnma*) with lattice parameters related to those of the ideal cubic subcell as $a\approx c\approx a_p\sqrt{2}$ and $b\approx 2a_p$.[10,11] Due to the pseudocubic character of the lattice, x-ray diffraction patterns at ambient conditions have rather symmetric peaks (Fig. 1). With a pressure increase, the diffraction peak formed by (202) and (040) reflections and located at $2\theta=21.5°$ splits into two peaks, indicating a noticeably larger compressibility of the *b* lattice parameter in comparison with those of *a* and *c* (Fig. 2). The compression anisotropy can be characterized by "orthorhombic" strains $Os_{\parallel}=2(c-a)/(c+a)$ in the (*ac*) plane and $Os_{\perp}=2(a+c-b\sqrt{2})/(a+c+b\sqrt{2})$ along the *b* axis.[29] The $Os_{\parallel}$ increases nearly linearly under pressure, while $Os_{\perp}$ grows more rapidly and exhibits a slope change at $P\sim 20$ GPa (Fig. 2). The qualitatively similar behavior of orthorhombic strains was also observed in $La_{0.5}Ca_{0.5}MnO_3$ with the CE-type AFM ground state, although a slope change of $Os_{\perp}$ was found at a considerably smaller pressure $P=5$ GPa.[21] The unit cell volume versus pressure dependence does not show any signatures (Fig. 2). The volume compressibility data of $La_{0.33}Ca_{0.67}MnO_3$ (Fig. 2) were fitted by the Birch–Murnaghan equation of state.[30] The value $B_0=235(5)$ GPa calculated with the fixed $B'=4.0$ and $V_0=216.5$ Å^3 is somewhat larger than $B_0=186$ GPa obtained for $La_{0.5}Ca_{0.5}MnO_3$ (Ref. 21) and 178 GPa for $La_{0.75}Ca_{0.25}MnO_3$ (Ref. 29). No evidence of a monoclinic lattice distortion was found in the studied pressure range of 0–50 GPa at ambient temperature, unlike in the $La_{0.5}Ca_{0.5}MnO_3$ case.[21]

Neutron diffraction patterns of $La_{0.33}Ca_{0.67}MnO_3$ measured at selected pressures and temperatures are shown in Fig. 3. The structural parameters obtained at ambient conditions (Table I) are close to those from Refs. 10 and 11. At ambient pressure below $T_{N\text{-}WC}=140$ K, the appearance of magnetic lines (2/3 1 1/2) at 4.94 Å and (1/3 1 1/2) at 5.74 Å was observed, indicating an onset of the WC AFM state with a propagation vector $k_{WC}=(1/3\ 0\ 1/2)$.[10,11] The magnetic supercell of this AFM structure is tripled along *a* and doubled along *c* crystallographic axes $(3a\times b\times 2c)$, with its complex magnetic arrangement and relevant $d(3x^2-r^2)/d(3z^2-r^2)e_g$ orbital order of Mn^{3+} sublattice[10] shown in Fig. 4. In addition, the appearance of a magnetic peak (1/2 1 1/2) characteristic of the *C*-type AFM state[11] with a propagation vector $k_C=(1/2\ 0\ 1/2)$ was detected below $T_{N\text{-}C}=155$ K. The magnetic supercell of this AFM structure is doubled along the *a* and *c* crystallographic axes $(2a\times b\times 2c)$, with its magnetic arrangement and characteristic $d(3z^2-r^2)e_g$ orbital order also shown in Fig. 4. A coexistence of WC and *C*-type AFM states for $x\sim 2/3$ was also previously observed at ambient pressure.[10,11] One should note that at ambient pressure, the *C*-type AFM state is a ground state of the $La_{1-x}Ca_xMnO_3$ system for $x\sim 0.85$, and its onset is

TABLE I. Structural parameters of $La_{0.33}Ca_{0.67}MnO_3$ at selected pressures and temperatures obtained from neutron diffraction experiment. In the orthorhombic phase of *Pnma* symmetry, the atomic positions are La/Ca1 and $O1_a$−4(b) (x, 0.25, z), Mn1−4(a) (0.5, 0, 0), and $O1_p$−8(d) (x, y, z). In the monoclinic space group of $P2_1/m$ symmetry, the atomic positions are: La/Ca1,2 and $O1,2_a$−2(e) (x, 0.25, z), Mn1−2(b) (0.5, 0, 0), Mn2−2(c) (0, 0, 0.5) and $O1,2_p$−4(f) (x, y, z).

P (GPa)	0	2.3		5.0	
T (K)	290	290	10	290	10
Space group	*Pnma*	*Pnma*	$P2_1/m$	*Pnma*	$P2_1/m$
a (Å)	5.376(3)	5.364(4)	5.371(4)	5.350(4)	5.337(5)
b (Å)	7.584(5)	7.542(6)	7.416(6)	7.492(6)	7.370(7)
c (Å)	5.385(5)	5.374(5)	5.383(5)	5.362(6)	5.368(5)
β (deg)			92.1(2)		92.8(2)
La/Ca1 x	0.024(1)	0.024(2)	0.053(2)	0.054(3)	0.042(2)
z	0.007(2)	−0.011(3)	0.004(3)	−0.014(4)	0.019(3)
La/Ca2 x			0.514(2)		0.492(2)
z			0.482(3)		0.479(3)
$O1_a$ x	0.495(2)	0.480(5)	0.463(5)	0.475(5)	0.483(5)
z	0.059(2)	0.034(5)	0.054(5)	0.043(5)	0.049(5)
$O2_a$ x			0.964(5)		0.970(5)
z			0.448(5)		0.463(5)
$O1_p$ x	0.281(3)	0.273(5)	0.276(5)	0.269(5)	0.268(5)
y	0.030(1)	0.038(3)	0.033(4)	0.033(3)	0.035(4)
z	0.719(3)	0.727(5)	0.724(5)	0.731(5)	0.732(5)
$O2_p$ x			0.768(5)		0.772(5)
y			0.030(4)		0.020(4)
z			0.768(5)		0.772(5)
R_p (%)	5.92	6.95	9.75	7.84	8.59
R_{wp} (%)	4.45	6.25	7.55	8.51	6.57

accompanied by a subtle monoclinic lattice distortion (angle $\beta \approx 91°$).[11,31] At low temperature, due to a limited resolution of the diffractometer used, it was difficult to resolve the monoclinic distortion of the *C*-type AFM phase and full structural parameters sets in coexisting AFM phases. The lattice parameters of WC and *C*-type AFM phases were found to have close values: $a \approx 5.410(3)$ Å, $b \approx 7.526(5)$ Å, $c \approx 5.417(3)$ Å at $T=10$ K. The observed noticeable shrinkage of the b lattice parameter and some elongation of a and c lattice parameters at low temperature for WC and *C*-type AFM phases in comparison with those for the paramagnetic phase at ambient temperature (Table I) is in agreement with previous studies of the $La_{1-x}Ca_xMnO_3$ system.[10,11,31] The magnetic structure refinements for the *C*-type AFM state were performed with orthogonal crystallographic axes corresponding to $\beta=90°$. The values of ordered Mn magnetic moments in WC and *C*-type AFM states (averaged for Mn^{3+} and Mn^{4+} sublattices for the WC AFM state, which have close magnetic moment values) at $T=10$ K are $\mu_{WC} \approx \mu_C = 1.1(1)$ μ_B, implying that their volume fractions are almost the same. It is reasonable to assume that coexisting WC and *C*-type AFM states form domains of nanoscopic size, as found for $La_{1-x}Ca_xMnO_3$ ($x=0.67-0.77$).[32,33]

At $P \geqslant 2$ GPa, on cooling, the intensity of the strongest magnetic lines (2/3 1 1/2) and (1/3 1 1/2) from the WC AFM state was fully suppressed, while the intensity of the (1/2 1 1/2) magnetic line from the *C*-type AFM state increases noticeably (Fig. 3). This corresponds to the total suppression of the WC AFM state in favor of the *C*-type AFM one. The value of the ordered magnetic moment at $T=10$ K is about the same, $\mu_C \approx 2.2(1)$ μ_B, over 2–5 GPa pressure range. The $T_{N\text{-}C}$ value significantly increases from 155 to 235 K in the 0–2 GPa pressure range (Fig. 5). No further changes in diffraction patterns were found at high pressures up to 5 GPa, indicating the stability of the *C*-type AFM state. The structural parameters of $La_{0.33}Ca_{0.67}MnO_3$ obtained from a Rietveld refinement of diffraction data at selected pressures and $T=10$ K, using a monoclinic structural model of $P2_1/m$ symmetry,[11,31] are listed in Table I.

In the orthorhombic paramagnetic phase of $La_{0.33}Ca_{0.67}MnO_3$ (Table I), the MnO_6 octahedra consist of a pair of apical Mn-$O1_a$ bond lengths oriented along the b axis and two pairs of inequivalent planar Mn-$O1_p$ bond lengths lying in (ac) planes, having rather close values $l_{Mn\text{-}O1a} = 1.923(5)$ Å and $l_{Mn\text{-}O1p(1,2)} \approx 1.930(5)$ Å at ambient conditions. The compression of MnO_6 octahedra at ambient tem-

perature is anisotropic with the most compressible Mn-O1$_a$ bond (Fig. 5). Its linear compressibility $k_{\text{Mn-O}i}=-[1/(l_{\text{Mn-O}i})_{P=0}](dl_{\text{Mn-O}i}/dP)_T$ is $k_{\text{Mn-O1}a}=0.004$ GPa^{-1}, while the corresponding value for the average of Mn-O1$_p$ bonds is about twice smaller, $k_{\langle\text{Mn-O1}p\rangle}=0.002$ GPa^{-1}. The average ⟨Mn-O-Mn⟩ bond angle increases from 160.5° to 164.8° in the 0–5 GPa pressure range.

The onset of the *C*-type AFM state is accompanied by a monoclinic lattice distortion, leading to a cooperative apical elongation of manganese octahedra along (1 0 1) directions due to $d(3z^2-r^2)e_g$ orbital ordering (Fig. 4). In the monoclinic low temperature phase of $La_{0.33}Ca_{0.67}MnO_3$ (Table I), there are two different types of manganese octahedra Mn(1,2)O$_6$, consisting of the pair of apical Mn(1,2)-O(1,2)$_a$ and two pairs of planar Mn(1,2)-O(1,2)$_p$ bond lengths, respectively. At $P=2.3$ GPa and $T=10$ K, the apical Mn1-O1$_a$, Mn2-O2$_a$ and planar Mn1-O1$_p$, Mn2-O1$_p$ distances have rather close values $l_{\text{Mn1-O1}a}\approx l_{\text{Mn-O2}a}\approx 1.886(6)$ and $l_{\text{Mn1-O1}p}\approx l_{\text{Mn2-O1}p}\approx 1.893(6)$ Å, while the remaining planar Mn1-O2$_p$ and Mn2-O2$_p$ distances are noticeably longer, $l_{\text{Mn1-O2}p}\approx l_{\text{Mn2-O2}p}\approx 1.952(7)$ Å. At high pressures and $T=10$ K, the compressibility of shorter

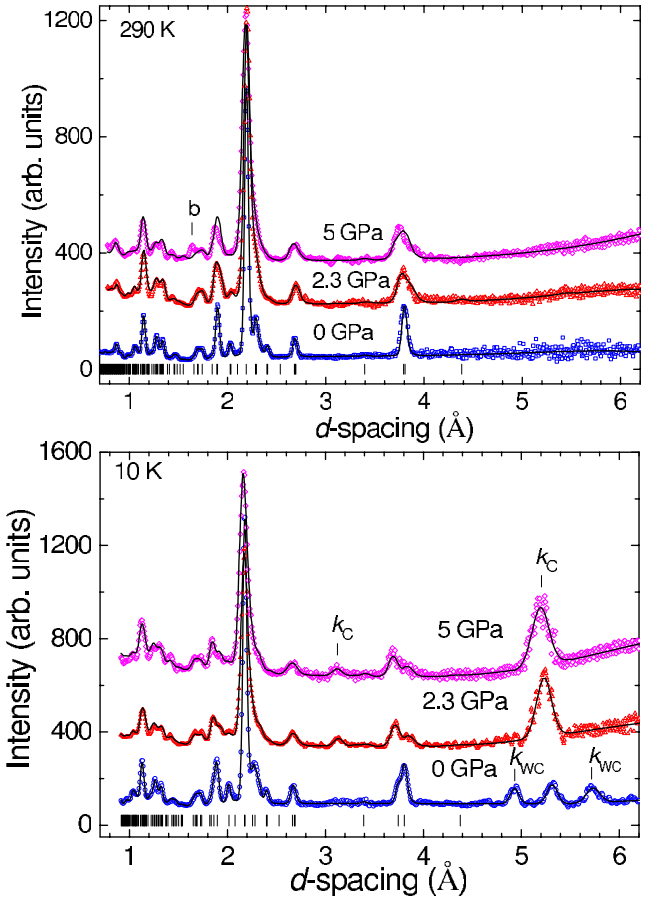

FIG. 3. (Color online) Neutron diffraction patterns of $La_{0.33}Ca_{0.67}MnO_3$ measured at different pressures and temperatures and processed by the Rietveld method. Ticks below represent calculated positions of nuclear peaks. Most intense magnetic peaks from WC and *C*-type AFM structures are marked as k_C and k_{WC}, respectively. The background peak from a high pressure cell is marked as "b."

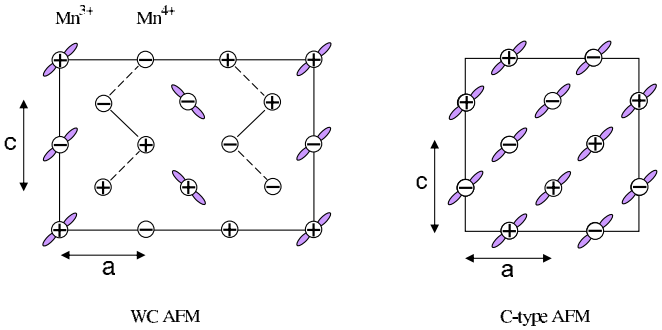

FIG. 4. (Color online) Schematic representation of Mn magnetic moment arrangement and e_g orbital order in Wigner-crystal AFM structure with a propagation vector $k_{WC}=(1/3\ 0\ 1/2)$ and *C*-type AFM structure with a propagation vector $k_C=(1/2\ 0\ 1/2)$. "+" and "−" correspond to FM and AFM couplings between neighboring Mn magnetic moments, which are located in (*ac*) planes and AFM coupled along the *b* axis. The conventional and frustrated Mn^{4+}-O^{2-}-Mn^{4+} superexchange interactions in WC AFM phase are shown by solid and dashed lines.

Mn(1,2)-O(1,2)$_a$ and Mn(1,2)-O1$_p$ bond lengths is about the same, $k_{\text{Mn(1,2)-O(1,2)}a}\approx k_{\text{Mn(1,2)-O1}p}\approx 0.0047$ GPa^{-1}, while that for the longer Mn(1,2)-O2$_p$ bond lengths is considerably smaller, $k_{\text{Mn(1,2)-O2}p}\approx 0.0008$ GPa^{-1}. This implies a further elongation of manganese octahedra at high pressure in the monoclinic low temperature phase.

In the limit of small pressures, the Clausius–Clapeyron equation $dT_t/dP=\Delta S/\Delta V$, where ΔS and ΔV are the entropy and volume changes at transition temperature T_t, predicts a positive pressure coefficient for the charge ordering temperature $dT_{CO}/dP\approx 2.5$ K/GPa, calculated using unit cell volume[10] and specific heat data[34] at ambient pressure and, therefore, a stability of the AFM WC state. The relevant compound $La_{0.5}Ca_{0.5}MnO_3$, indeed, follows such a prediction and the CE-type AFM state remains stable at high pressures of up to at least 6.2 GPa with $dT_{CO}/dP\sim dT_N/dP\sim 4$ K/GPa.[21] In contrast, the WC AFM state of $La_{0.33}Ca_{0.67}MnO_3$ is rapidly suppressed at high pressures.

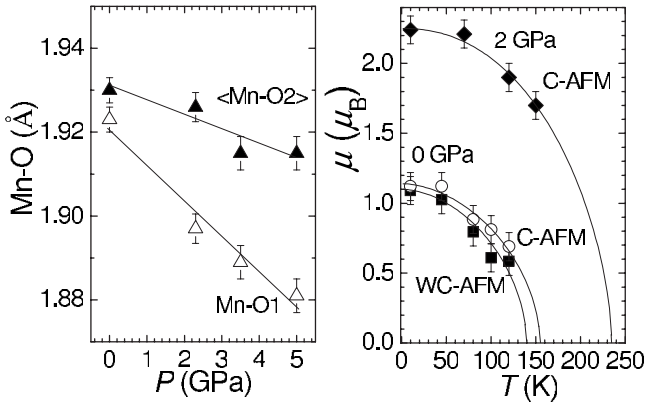

FIG. 5. Left: Mn-O bond lengths in the orthorhombic phase of $La_{0.33}Ca_{0.67}MnO_3$ as functions of pressure at ambient temperature. Right: Temperature dependences of Mn magnetic moments of WC AFM (averaged among Mn^{3+} and Mn^{4+} sublattices) and *C*-type AFM phases for $P=0$ and 2 GPa.

Such a behavior can be attributed to the following reasons. First, the application of a high pressure leads to an increase in the e_g electron transfer electron integral[35] $t \sim \cos(1/2[\pi\text{-}\langle\text{Mn-O-Mn}\rangle])/l^{3.5}_{\langle\text{Mn-O}\rangle}$ in the Mn^{3+}-O^{2-}-Mn^{4+} network and an enhanced delocalization of e_g electrons participating in the conduction process. While in the WC AFM state, due to a peculiar orbital order (Fig. 4), the e_g electron transfer is possible along quasi-one-dimensional zigzag Mn^{3+}-O^{2-}-Mn^{4+} FM chains only; in the *C*-type AFM state, such a transfer is realized along (101) ferromagnetic linear chains (Fig. 4), resulting in a higher kinetic energy gain[36] and making the *C*-type AFM state more energetically preferable at high pressures. Second, in the framework of a charge ordered model of the WC AFM structure of $La_{0.33}Ca_{0.67}MnO_3$, there exists a number of frustrated magnetic Mn^{4+}-O^{2-}-Mn^{4+} interactions (Fig. 4), which have AFM coupling along the *b* axis and either AFM or FM coupling in (*ac*) planes, and such a frustration presumably induces some spin canting.[10] Such interactions should naturally be AFM in accordance with Goodenough–Kanamori rules, as is observed in most of the oxides containing Mn^{4+} ions and predicted by theoretical considerations.[37] The increase in superexchange interaction strength[38] $J_{AF} \sim t^4$ at high pressure is expected to remove the frustration of Mn^{4+}-O^{2-}-Mn^{4+} interactions and result in the instability of the WC AFM structure. These considerations are consistent with a recent theoretical study,[39] which showed that the AFM phase with a zigzag chain topology of orbital and magnetic order in manganites is realized for the $x \sim 2/3$ concentration only in a narrow range of J_{AF}/t values and it is unstable with respect to the *C*-type AFM phase for a decrease in λ/t value (the parameter λ characterizes the electron-phonon coupling strength).

One should note that high pressure effects in $La_{0.33}Ca_{0.67}MnO_3$ are qualitatively similar to chemical composition effects related to an increase in $\langle r_A \rangle$ in $R_{0.33}A_{0.67}MnO_3$. In the latter case, also a decrease in average bond length $l_{\langle\text{Mn-O}\rangle}$, an increase in average bond angle $\langle$Mn-O-Mn$\rangle$ values, and a change in ground state from WC AFM observed in $La_{0.33}Ca_{0.67}MnO_3$ (a similar state is also found in $Pr_{0.33}Ca_{0.67}MnO_3$) to a *C*-type AFM one (observed in $Nd_{0.33}Sr_{0.67}MnO_3$, $Pr_{0.33}Sr_{0.67}MnO_3$, and $La_{0.33}Sr_{0.67}MnO_3$) occur.[3–5,10,12]

IV. CONCLUSIONS

Our results demonstrate that the WC AFM state in $La_{0.33}Ca_{0.67}MnO_3$ is remarkably unstable at high pressures and is rapidly suppressed in favor of the *C*-type AFM state. Such a behavior is in sharp contrast to the stability of the WC AFM state in high magnetic fields of up to 14 T as well as the stability of the relevant CE-type AFM state in $La_{0.5}Ca_{0.5}MnO_3$ for a comparable pressure range. It can be related to enhanced e_g electron delocalization and superexchange interaction strength at high pressures.

ACKNOWLEDGMENTS

The financial support from BGI and RFBR, Grants Nos. 08-02-90018-Bel-a and 08-02-90427-Ukr-a, is gratefully acknowledged.

[1] *Colossal Magnetoresistance Oxides*, edited by Y. Tokura (Gordon and Breach, New York, 2000).
[2] E. Dagotto, T. Hotta, and A. Moreo, Phys. Rep. **344**, 1 (2001).
[3] O. Chmaissem, B. Dabrowski, S. Kolesnik, J. Mais, J. D. Jorgensen, and S. Short, Phys. Rev. B **67**, 094431 (2003).
[4] E. Pollert, Z. Jirák, J. Hejtmánek, A. Strejc, R. Kužel, and V. Hardy, J. Magn. Magn. Mater. **246**, 290 (2002).
[5] R. Kajimoto, H. Yoshizawa, H. Kawano, H. Kuwahara, Y. Tokura, K. Ohoyama, and M. Ohashi, Phys. Rev. B **60**, 9506 (1999).
[6] E. O. Wollan and W. C. Keller, Phys. Rev. **100**, 545 (1955).
[7] J. B. Goodenough, Phys. Rev. **100**, 564 (1955).
[8] P. G. Radaelli, D. E. Cox, M. Marezio, and S.-W. Cheong, Phys. Rev. B **55**, 3015 (1997).
[9] C. H. Chen, S.-W. Cheong, and H. Y. Hwang, J. Appl. Phys. **81**, 4326 (1997).
[10] P. G. Radaelli, D. E. Cox, L. Capogna, S.-W. Cheong, and M. Marezio, Phys. Rev. B **59**, 14440 (1999).
[11] M. Pissas and G. Kallias, Phys. Rev. B **68**, 134414 (2003).
[12] Z. Jirák, C. Martin, M. Hervieu, and J. Hejtmánek, Appl. Phys. A: Mater. Sci. Process. **74**, S1755 (2002).
[13] F. Millange, S. de Brion, and G. Chouteau, Phys. Rev. B **62**, 5619 (2000).
[14] T. Hotta, Y. Takada, H. Koizumi, and E. Dagotto, Phys. Rev. Lett. **84**, 2477 (2000).
[15] A. Daoud-Aladine, J. Rodriguez-Carvajal, L. Pinsard-Gaudart, M. T. Fernandez-Diaz, and A. Revcolevschi, Phys. Rev. Lett. **89**, 097205 (2002).
[16] J. Herrero-Martín, J. García, G. Subías, J. Blasco, and M. Concepcion Sánchez, Phys. Rev. B **70**, 024408 (2004).
[17] M. Coey, Nature (London) **430**, 155 (2004).
[18] J. C. Loudon, S. Cox, A. J. Williams, J. P. Attfield, P. B. Littlewood, P. A. Midgley, and N. D. Mathur, Phys. Rev. Lett. **94**, 097202 (2005).
[19] J. C. Loudon, L. F. Kourkoutis, J. S. Ahn, C. L. Zhang, S.-W. Cheong, and D. A. Muller, Phys. Rev. Lett. **99**, 237205 (2007).
[20] X. G. Li, R. K. Zheng, G. Li, H. D. Zhou, R. X. Huang, J. Q. Xie, and Z. D. Wang, Europhys. Lett. **60**, 670 (2002).
[21] D. P. Kozlenko, L. S. Dubrovinsky, I. N. Goncharenko, B. N. Savenko, V. I. Voronin, E. A. Kiselev, and N. V. Proskurnina, Phys. Rev. B **75**, 104408 (2007).
[22] A. Arulraj, R. E. Dinnebier, S. Carlson, M. Hanfland, and S. van Smaalen, Phys. Rev. Lett. **94**, 165504 (2005).
[23] N. A. Dubrovinskaia and L. S. Dubrovinsky, Rev. Sci. Instrum. **74**, 3433 (2003).
[24] A. P. Hammersley, S. O. Svensson, M. Hanfland, A. N. Fitch, and D. Hausermann, High Press. Res. **14**, 235 (1996).
[25] A. C. Larson and R. B. Von Dreele, General Structure Analysis System (GSAS), Los Alamos National Laboratory Report No. LAUR 86-748, 1994.

[26] V. P. Glazkov and I. N. Goncharenko, High Pressure Physics and Technics **1**, 56 (1991) (in Russian).
[27] V. B. Zlokazov and V. V. Chernyshev, J. Appl. Crystallogr. **25**, 447 (1992).
[28] J. Rodríguez-Carvajal, Physica B **192**, 55 (1993).
[29] C. Meneghini, D. Levy, S. Mobilio, M. Ortolani, M. Nuñez-Reguero, A. Kumar, and D. D. Sarma, Phys. Rev. B **65**, 012111 (2001).
[30] F. J. Birch, J. Geophys. Res. **91**, 4949 (1986).
[31] M. Pissas, G. Kallias, M. Hofmann, and D. M. Többens, Phys. Rev. B **65**, 064413 (2002).
[32] J. Tao and J. M. Zuo, Phys. Rev. B **69**, 180404(R) (2004).
[33] J. Tao, D. Niebieskikwiat, M. B. Salamon, and J. M. Zuo, Phys. Rev. Lett. **94**, 147206 (2005).
[34] T. Qian, R. K. Zheng, T. Zhang, T. F. Zhou, W. B. Wu, and X. G. Li, Phys. Rev. B **72**, 024432 (2005).
[35] W. A. Harrison, *The Electronic Structure and Properties of Solids* (Freeman, San Francisco, CA, 1980).
[36] J. van den Brink, G. Khaliullin, and D. Khomskii, Phys. Rev. Lett. **83**, 5118 (1999).
[37] J. B. Goodenough, *Magnetism and the Chemical Bond* (Interscience, New York, 1963).
[38] J.-S. Zhou and J. B. Goodenough, Phys. Rev. B **68**, 054403 (2003).
[39] L. Brey, Phys. Rev. Lett. **92**, 127202 (2004).